Strain-engineering Induced Anisotropic Crystallite Orientation and Maximized Carrier Mobility for High-performance Microfiber-based Organic Bioelectronic Devices

Youngseok Kim[1], Hyebin Noh[1], Bryan D. Paulsen[2], Jiwoong Kim[1], Il-Young Jo[1], HyungJu Ahn[3], Jonathan Rivnay[2,4]*, and Myung-Han Yoon[1]**

[1]School of Materials Science and Engineering, Gwangju Institute of Science and Technology, Gwangju 61005, Republic of Korea

[2]Department of Biomedical Engineering, Northwestern University, IL 60208 USA

[3]Industrial technology convergence center, Pohang Accelerator Laboratory, POSTECH, Pohang, Gyeongbuk 37673, Republic of Korea

[4]Simpson Querrey Institute, Northwestern University, IL 60611 USA

*Corresponding authors: Dr. Hyungju Ahn, Prof. Jonathan Rivnay, and Prof. Myung-Han Yoon

E-mail: hyungju@postech.ac.kr, jrivnay@northwestern.edu, and mhyoon@gist.ac.kr

Keywords: strain engineering, organic electrochemical transistors, PEDOT:PSS, conducting polymers, mixed conductors

Abstract

Despite the importance of carrier mobility, recent research efforts have been mainly focused on the improvement of volumetric capacitance in order to maximize the figure-of-merit, μC^* (product of carrier mobility and volumetric capacitance) for high-performance organic electrochemical transistors. Herein, we report high-performance microfiber-based organic electrochemical transistors with unprecedentedly large μC^* using highly-ordered crystalline PEDOT:PSS microfibers with very high carrier mobilities. The strain engineering via uniaxial tension was employed in combination with solvent-mediated crystallization in the course of drying coagulated fibers, resulting in the permanent preferential alignment of crystalline PEDOT:PSS domains along the fiber direction which was verified by atomic force microscopy and transmission wide-angle x-ray scattering. The resultant strain-engineered microfibers exhibited very high carrier mobility (12.9 $cm^2 V^{-1} s^{-1}$) without the trade-off in volumetric capacitance (122 F cm^{-3}) and hole density (5.8×10^{20} cm^{-3}). Such advantageous electrical and electrochemical characteristics offered the bench-mark parameter of μC^* over ~1500 F $cm^{-1}V^{-1}s^{-1}$, which is the highest metric ever reported in the literature and could be beneficial for realizing a new class of substrate-free fibrillar and/or textile bioelectronics in the configuration of electrochemical transistors and/or electrochemical ion pumps.

Introduction

Organic electrochemical transistors (OECTs) based on organic mixed ionic-electronic conductors (OMIECs) show large signal amplification in the presence of aqueous electrolytes[1]. This characteristic made OECTs advantageous for many bioelectronic applications, for instance, implanted electronics[2–7], chemical sensors[8–11], cellular interfaces[12–15] and stretchable sensors [16–18] where it is desired to amplify small electrical/electrochemical signals in aqueous environments and/or under mechanical strain/deformation. To realize high-performance OECT devices even with small feature sizes and low operating voltages, aqueous ions driven by the gate bias should efficiently penetrate into the OMIEC for doping/dedoping the channel material, while the modulated charge carriers should effectively transport through the conjugated polymer-based channel by the potential applied between source and drain electrodes. Accordingly, both large volumetric capacitance (C^*) and high carrier mobility (μ) of the OMIEC channel material lead to high transconductance (g_m) in a given OECT, thus, their product (μC^*) is employed as a figure of merit to benchmark OECT performance.

Various types of OMIEC materials have been proposed by deliberately incorporating ionically-permeable side chains into electrically conductive conjugated polymers not only for developing high-performance bioelectronics but also for studying their fundamental mechanism.[19] These materials contributed to the improvement of accumulation-mode OECT operation by controlling energy levels and film morphology[20–24] as well as the realization of unique device functions for enzymatic metabolite sensors[25] and complementary logic circuits.[26] In the course of searching for novel OMIEC materials and developing pre-/post-treatment methods, the most dominant strategy to maximize the performance figure-of-merit (*i.e.*, μC^* product) has been mainly focused on the route to efficient channel doping/dedoping capability, which is represented by the efforts made for increasing C^*. For instance, it was reported that the judicious incorporation of water-swelling side chains and/or polymer additives into conjugated polymer cores leads to the μC^* product of the corresponding channel film over 260 F cm^{-1}V^{-}

$^{1}s^{-1}$ (*e.g.*, p(g2T-TT))[27]. In parallel, poly(3,4-ethylenedioxythiophene):polystyrene sulfonate (PEDOT:PSS) has been one of the most frequently studied materials for OECTs and bioelectronics due to high electrical conductivity, good ambient stability, solution-processability, and commercial availability, as justified by the decent benchmark parameter (μC^*) of 47 F $cm^{-1}V^{-1}s^{-1}$ for the pristine PEDOT:PSS[28]. More recently, it was demonstrated that the removal of excessive water-swelling dopant (*i.e.*, PSS) out of the as-deposited PEDOT:PSS channel could boost up the volumetric capacitance up to 113 F cm^{-3} as well as enhance water stability, leading to a very large μC^* product of 490 F $cm^{-1}V^{-1}s^{-1}$.[29] In this case, the removal of extra PSS which was not associated with either doping or ion conduction pathway resulted in the substantial reduction of film thickness, thus, volume, and the consequent volume-normalized capacitance (C^*) was significantly enlarged. Nonetheless, relatively fewer efforts have been made to enhance carrier mobility (μ) although it is one of the two key parameters to improve OECT performance in terms of current modulation efficiency or transconductance. This could be partly because carrier mobility has been regarded as an intrinsic material property which is relatively difficult to customize other than by molecular design.

Herein, we developed high-performance microfiber-based organic electrochemical transistors with unprecedentedly large carrier mobility (12.9 cm^2 V^{-1} s^{-1}) and μC^* product (1500 F $cm^{-1}V^{-1}s^{-1}$) using highly-ordered crystalline PEDOT:PSS microfibers. A geometrically well-defined one-dimensional microfiber structure was chosen as an OECT channel to reduce dimensional complexity, while strain engineering which is a general strategy employed in semiconductor manufacturing was introduced to enhance the microstructural ordering in the channel material. For the strain engineering of mixed conductor microfibers, the uniaxial tension in combination with solvent-mediated crystallization was employed in the course of drying coagulated fibers, resulting in the permanent preferential alignment of crystalline PEDOT domains along the fiber direction. The resultant changes in solid-state microstructure and surface morphology were investigated by transmission wide-angle x-ray scattering and atomic force

microscopy, respectively. The corresponding microfiber-based OECTs with gradually-modulated crystallite orientations were thoroughly characterized to extract the electrical/electrochemical properties such as volumetric capacitance, charge carrier density, and carrier mobility. Lastly, we propose the underlying molecular mechanism of one-dimensionally highly-oriented PEDOT:PSS crystallite alignment and highly-enhanced charge transport efficacy, and discuss their potentials for high-performance substrate-free bioelectronics based on microfibrillar OMIECs.

Results and Discussion

Microfibers were prepared by the conventional wet-spinning process which has been well customized in terms of spinning, post-treatment, rinsing/drying for conducting polymer-based (micro)fibers targeting at textile electronics.[30–35] In this study, PEDOT:PSS solution was cylindrically coagulated via wet-spinning in acetone (ACE), followed by the post-treatment by dipping in sulfuric acid (SA) (see the Method section for the details). As shown Figure 1a, SA-treated microfibers were fabricated by dipping as-spun fibers (*i.e.*, ACE-treated microfibers) into sulfuric acid. For strain engineering, these as-prepared *wet* fibers were dried under tension (T) by hanging a metal wire with the known mass (m) at one end (Figure 1b). The exerted tension was represented by gravitational force ($W = mg$, $g = 9.8\ \mathrm{m{\cdot}s^2}$) and converted to stress (σ) by dividing it by the cross-sectional area of a given microfiber (A). After drying, scanning electron microscopy (SEM) images of the strain-engineered microfibers were obtained as shown in the Figure 1c, to confirm that well-defined circular-shaped microfiber structure. The resultant SA- and ACE-treated microfibers showed diameters ranging from 10 to 15 μm and from 13 to 20 μm, respectively, depending on the applied stress (Figure S1). Note that the stress applied during the drying process was denoted as T/A so that it can be differentiated from other parameters with the same notation such as electrical conductivity.

To investigate the mechanical behaviors of strain-engineered microfibers, the stress-strain curves were obtained using representative strain-engineered SA-treated microfibers. As shown in Figure 1d, the increase in the applied *T/A* from 10.8 kPa to 13.0 MPa led to the gradual increase in mechanical modulus and fracture stress from 0.95 to 8.7 GPa and from 147 to 312 MPa, respectively, but the decrease in fracture strain from 47 to 8.7% (Figure S2). As shown in the electrical conductivities of strain-engineered microfibers measured at the contact pad geometry of four-point probe (Figure 1e), SA-treated microfibers showed much higher electrical conductivities than ACE-treated microfibers which underwent only the ACE treatment during the coagulation. This is because the solvent-mediated crystallization via SA treatment effectively removes excess PSS chains from PEDOT:PSS microfibers as verified by the residual PSS/PEDOT ratio obtained from the x-ray photoelectron microscopy (XPS, Figure S3) analysis. Interestingly, both SA- and ACE-treated PEDOT:PSS microfibers exhibited the substantial enhancement in electrical conductivity which is proportional to the applied *T/A*, suggesting that strain-engineering is not limited to SA-treated microfibers and, in principle, can be generalized to modulate mechanical/electrical/electrochemical properties of other polymer microfibers.

Figure 2a and b show the atomic force microscopy (AFM) images of and the two-dimensional transmission wide angle x-ray diffraction (2D TR-WAXD) spectra of representative strain-engineered SA-treated microfibers (*T/A*= 42k, 380k, 2.1M, and 61 MPa). Note that detailed information on measurements are described in the Method section. As higher *T/A* was applied during the drying process of SA-treated PEDOT:PSS microfibers, the grain sizes on the fiber surface remained unchanged but their overall orientations were gradually aligned along the fiber direction (see the red arrow in Figure 2a, i). The similar trend was observed in 2D TR-WAXD patterns. With the increased *T/A,* the peak intensities became more prominent at q = 1.8 and 0.5 $Å^{-1}$ (d = 3.5 and 12.6 Å) which represent the π-π stacking (020) and lamellar structure (100) of PEDOT chains, respectively. Note that these results are closely correlated with electrical conductivities of PEDOT:PSS microfibers (*vide infra*). More interestingly, as

132 the applied *T/A* was increased, the isotropic ring pattern was gradually switched to the horizontally
133 polarized pattern with increased peak intensities, which suggests that the overall isotropic structure with
134 random crystallite orientation was replaced by the anisotropic structure with preferential crystallite
135 orientation along the fiber direction. For the in-depth analysis, the diffraction intensity profiles through
136 vertical (ψ = 90°) and horizontal (ψ = 0°; red arrow in Figure 2b, i) axis were plotted in Figures 2c and
137 d, respectively. With the increased *T/A,* the peaks corresponding to the π-π stacking (q = 1.8 Å^{-1}) and
138 lamellar structure (q = 0.5 Å^{-1}) were enhanced/diminished in the vertical/parallel direction without
139 significant peak shift (i.e., no crystal lattice distortion). The minor peak at q = 1.65 Å^{-1} (d = 3.8 Å) due
140 to the repeating unit of PEDOT chains (*e.g.*, aromatic ring) were slightly amplified along the fiber
141 direction, as the applied *T/A* was increased.[30] Also, the amorphous halo peak attributed to PSS chains
142 near q = 1.2 Å^{-1} (d = 5.2 Å) merged into four mixed-index peaks with the increased tensile stretching,
143 suggesting that not only the PEDOT chains but also PSS chains were aligned along the fiber direction by
144 the tensile stress in the course of microfiber drying. The 2D TR-WAXD patterns and diffraction intensity
145 profiles of strain engineered ACE-treated PEDOT:PSS microfibers indicate that the similar
146 microstructural reorganization could be induced by the increased *T/A* but to a lesser extent (Figure S4).
147 For comparison, the domain size (L_{020}) and the inter-chain distance (d_{020}) attributed to the π-π stacked
148 PEDOT chains were extracted from the vertical (ψ = 90°) line-cut profiles of strain-engineered SA- and
149 ACE-treated microfibers (Figure 2e). It is noteworthy that the SA-treated microfibers showed larger L_{020}
150 and smaller d_{020} than ACE-treated microfibers, but these metrics were not changed significantly (<10%)
151 by the applied stress, even though the applied tensile stress made significant changes in domain
152 orientation. We suppose that although the tensile stress was exerted on wet microfibers which were
153 partially swollen with water molecules prior to the complete establishment of crystallization, the crystal
154 domains were aligned along the fiber direction without severe disturbance in molecular ordering via π-π
155 stacking. Note that considering that the anisotropic crystallite ordering in PEDOT:PSS microfibers can

be gradually generated during the drying process under the tensile stress, our results are distinct from those in the previous literature where it is argued that the crystalline domains of PEDOT chains could be creeped and slid during the mechanical winding process of PEDOT:PSS fibers[31]. Lastly, the degree of orientation of PEDOT and PSS chains were examined by analyzing the full-with half-maximum (FWHM) values in azimuthal intensity profiles of (100) and (020) peaks (Figure 2f). This result clearly shows that the PEDOT and PSS chains are gradually aligned along the fiber direction by increasing the applied tensile stress.

Prior to the further characterization of microfibers, we examined the swelling behavior of strain-engineered PEDOT:PSS microfibers by exposing microfibers to water in a fluidic channel[32] (see the details in the Method section and Figure S5a, b), since swelling behaviors of microfibers may affect not only the fiber dimension change during the OECT operation but also the extraction of the corresponding volumetric capacitance. The microscopy images of microfibers were taken and processed using ImageJ software to extract the length (L) and diameter (D) of a given fiber at each state and the radial, axial, and volume swelling ratios (*i.e.*, L_{wet}/L_{dry}, D_{wet}/D_{dry} and V_{wet}/V_{dry}, respectively) were calculated (Figure S5c-e). In the case of ACE-treated microfibers (blue), as larger *T/A* was applied on the microfiber, the radial/axial swelling was gradually increased/decreased. In contrast, SA-treated microfibers (red) showed almost constant values (~ 1) of radial and axial swelling regardless of the applied *T/A*, indicating that there is no significant change in dimensions even after immersion in water. Interestingly, the resultant volume swelling changes of 47.9 ± 4.5 and 1.38 ± 0.22 for ACE- and SA-treated microfibers, respectively, were almost independent of the applied *T/A* and these values are well matched to those of ACE-(44) and SA-treated fibers (1.7) which were prepared without tensile stress[32]. Since excess PSS chains could be effectively removed by the SA treatment (Figure S3), the swelling in SA-treated PEDOT:PSS fibers should be minimal unlike ACE-treated microfibers where excess amount of residual PSS chains induces volumetric swelling and dimensional changes. Furthermore, as the crystallinity in

PSS becomes loose by water penetration (see the diminished PSS-related crystalline peaks in Figure S6), the elongated (PSS-rich) ACE-treated microfibers by the applied *T/A* tend to be relaxed back to the original as-spun microfibers by decreasing their lengths and increasing their diameters. Nonetheless, because the essential molecular-level microstructure was not changed by strain-engineering except for the crystallite orientation (*i.e.*, constant grain size and d-spacing regardless of the applied *T/A*, see Figure 2e-f and Figure 5), the volume swelling was apparently invariant regardless of the applied *T/A*.

To investigate the correlation between the microstructures and the electrical/electrochemical properties, organic electrochemical transistors (OECTs) were fabricated and characterized using strain-engineered PEDOT:PSS microfibers (Figure 3 and S7). An individual strain-engineered microfiber was connected with the strips of source and drain electrodes, on top of which the passivation layer was patterned for electrical insulation, while the active channel of PEDOT:PSS microfiber was covered with an aqueous electrolyte solution (100 mM NaCl) where a chlorinated silver electrode was immersed for gate biasing (Figure 3a, see also the experimental section for the details). Subsequently, the electrical/electrochemical properties of strain-engineered microfibers were extracted from OECT transfer/output and electrochemical impedance spectroscopy (EIS) measurements. Note that both OECT and EIS measurements were conducted using an identical microfiber device fabricated at a given *T/A* condition so that the obtained electronic/electrochemical properties (*e.g.*, carrier mobility and density) can be compared and/or crosschecked with each other. Figures 3b and c show the representative transfer and output curves from the strain-engineered microfiber OECT based on SA-treated PEDOT:PSS (*T/A*= 61 MPa). Despite the fibrillar channel with long channel length (L= 0.33 cm) and small cross-sectional area (A= 8.1 × 10^{-7} cm^2), the strain-engineered crystalline microfiber OECT showed clear switching and outstanding amplification performance as indicated by large on-current (~10^{-3} A), on-off current ratio (>10^3), and transconductance (~10^{-3} S) (see also Figure S8). Furthermore, there was no significant performance degradation during the on/off cycling (up to 500 times), and the repeated drying/wetting

processes (up to 8 times) (see Figures S9 and S10). Remarkably, the on-current values of strain-engineered microfiber OECTs gradually increased with the increased *T/A,* in both SA-treated (reddish lines) and ACE-treated PEDOT:PSS (blueish lines) (Figure 3d). Note that after L and A of microfiber used for OECT measurement were precisely measured, the current level in each transfer curve shown in Figure 3d was normalized by microfiber dimensions for fair comparison ($I_D^* = I_D \cdot L/A$).

For the in-depth investigation of the correlation between microstructural ordering and electrical/electrochemical properties, volumetric capacitance (C^*), hole density (p), pinch-off voltage (V_p) and carrier mobility (μ_{OECT}) were calculated from transfer curves and EIS spectra (Figure S11) based on Bernards-Malliaras model[33] using various stain-engineered PEDOT:PSS microfibers (Figures 3e-h) (The detailed information on parameter extraction is described in the supporting information). It was clearly demonstrated that only carrier mobility increased linearly in response to applied stress (T/A), while other extracted characteristics such as C^*, p, V_p remained almost constant with narrow statistical distributions (see dotted lines indicating upper and lower standard deviation limits in Figures 5e-h) regardless of the applied T/A. Considering that both C^* and p are related to the number of electrochemically doped PEDOT chains existing in the unit volume of microfiber channel, the C^* and p values of SA-treated microfibers which are larger 2 – 3 times than those of ACE-treated microfibers can be attributed to the increased PEDOT/PSS ratio due to the removal of unbound PSS via SA-treatment (Figure S3).[26] Furthermore, the marginal dependence of these two parameters on the applied T/A suggests that the doping density was not affected by mechanical stress during the drying process of both SA- and ACE-treated PEDOT:PSS microfibers. Similarly, V_p showed no correlation with the applied T/A in both SA- and ACE-treated PEDOT:PSS microfibers but the former showed much higher values than the latter. Note that V_p can be translated into the gate bias needed to dedope the doped-PEDOT chains, the charge density of which is equivalent to hole density (p), by attracting cations electrostatically ($C^* = p/V_p$). However, the efficiency of cation induction could be retarded when the crystallinity is escalated

228 in SA-treated PEDOT:PSS microfiber by PSS removal, leading to the substantial increase in V_p. The
229 correlation between microfiber crystallinity and cation penetration efficiency is also supported by the
230 observation that the π-π stacking ordering was preserved even after water immersion of SA-treated
231 PEDOT:PSS as shown in *ex-situ* x-ray diffraction results (Figure S6).

232 In contrast to volumetric capacitance (C^*), hole density (p), and pinch-off voltage (V_p), the carrier
233 mobility extracted from the strain-engineered SA-treated microfiber OECT measurement (μ_{OECT})
234 increased from 4.2 to 12.9 $cm^2 V^{-1} s^{-1}$ with the increased *T/A* was applied along the fiber direction (Figure
235 3h). As for electrical conduction, holes in the doped-PEDOT chains move along the conjugated polymer
236 chain (*intrachain transport*) and jump to the adjacent polymer chains by hopping (*interchain transport*).
237 Since charge carriers in an OECT transport typically through the randomly-oriented polymer channel by
238 finding the shortest pathway under electrical potential gradient, μ_{OECT} implies the geometrically-averaged
239 carrier mobility including both intrachain and interchain contributions, but it is commonly determined
240 by relatively low interchain transport. In the case of strain-engineered PEDOT:PSS microfibers, however,
241 the crystal domains of PEDOT chains are highly aligned along the fiber direction (Figure 2c), and the
242 resultant anisotropic directionality significantly increases the drift velocity of charge carrier under the
243 given potential gradient and, thereby, hole mobility. Furthermore, the strain-engineered microfiber
244 OECTs were investigated with a frequency-dependent bandwidth technique which allowed for the
245 alternative determination of charge carrier mobility from the hole transit time and the frequency
246 dependent transconductance (Figure S12).[15] The transconductance cut-off frequency (f_c) fell on the
247 order of 1 Hz for all PEDOT:PSS microfiber OECTs due to their relatively large channel dimensions,
248 while it was confirmed that the cut-off frequency is inversely proportional to the product of channel
249 thickness and the square root of nominal channel surface area (*i.e.*, $1/2\pi f_c \sim d(WL)^{1/2}$ for planar devices
250 and $1/2\pi\ f_c \sim d(2\pi rL)^{1/2}$ for fiber devices). Therefore, the product of cut-off frequency, channel thickness,
251 and square root of channel surface area ($f_c d(2\pi rL)^{1/2}$) was calculated to compare the frequency responses

of PEDOT:PSS microfiber OECT devices with different channel geometries. The strain-engineered SA- and ACE-treated PEDOT:PSS microfiber OECTs exhibited the values of ~2 × 10^{-5} and ~5 × 10^{-5}, respectively, which are comparable to those of the state-of-the-art PEDOT:PSS OECTs (10^{-5} – 10^{-4})[4,7,34–39]. This result suggests that, in principle, the strain-engineered PEDOT:PSS microfiber OECTs with reduced channel dimensions (*i.e.*, length and diameter) should be capable of excellent performance even at high frequencies. Furthermore, microfiber-based OECTs can show better frequency responses than thin-film-based ones due to the cylindrically-shaped channel which is essentially open for ionic diffusion/migration from all the radial direction, but it is also clear that highly crystalline microstructures in SA-treated PEDOT:PSS microfibers may impede ionic penetration into the channel, thus, retard frequency-dependent responses[28]. Note that the OECT mobilities extracted with the frequency-dependent bandwidth method ($\mu_{OECT,BW}$) showed the similar dependence on the applied *T/A* with the maximum values of 11.3 and 8.3 $cm^2 V^{-1} s^{-1}$ for SA- and ACE-treated PEDOT:PSS microfiber OECTs, respectively, at the *T/A* of 30 and 3.1 MPa.

As a figure-of-merit of OECT device performance, the μC^* product of strain-engineered PEDOT:PSS microfibers were plotted as a function of the applied *T/A* (Figure 4a). Since the carrier mobility is dramatically enhanced while the volumetric capacitance is maintained without undesired trade-off, the consequent $\mu_{OECT}C^*$ product of SA- and ACE-treated PEDOT:PSS microfibers exhibited the unprecedented enhancement from 549 to 1500 and from 180 to 445 F $cm^{-1}V^{-1}s^{-1}$, respectively. Note that $\mu_{OECT,BW}C^*_{BW}$ product of SA- and ACE-treated PEDOT:PSS microfibers exhibited similar maximum values, 1410 and 750 F $cm^{-1}V^{-1}s^{-1}$, respectively (Figure S13). To our knowledge, the μC^* product over 1500 F $cm^{-1}V^{-1}s^{-1}$ is the highest ever reported in the literature. Furthermore, for benchmarking purposes, the μ_{OECT} and C^* metrics of other previously reported mixed conductor materials[1] were plotted and compared with those of strain-engineered SA-treated PEDOT:PSS microfibers (Figure 4b and Table S1). The resultant scatter plot clearly demonstrates that the strain-

engineered crystalline PEDOT:PSS microfibers prepared with the *T/A* of 61 MPa exhibit the highest OECT carrier mobility (12.9 $cm^2 V^{-1} s^{-1}$) without the trade-off in volumetric capacitance (C^*), thus, the largest OECT figure-of-merit or μC^*.

Based on the abovementioned mechanical, microstructural, and electrical/electrochemical characterizations, we propose the following molecular scheme for the formation of crystalline PEDOT:PSS microfibers with and without strain-engineering (Figure 5). When an aqueous solution of PEDOT:PSS is injected into a polar solvent such as acetone and immediately treated with sulfuric acid for solvent-mediated crystallization, PEDOT:PSS becomes coagulated in the form of fiber and the excess amount of PSS chains are removed from the as-spun PEDOT:PSS microfiber. As shown in Figure 5a, during the drying process without the stress, free water molecules (pale blue) are evaporated first, while PSS chain-bound water molecules are evaporated more slowly due to the hydrophilic nature of PSS chains (Figure 5a, i). As the PSS chain-bound water molecules surrounding PSS chains (pale orange) are removed, the overall separation between PEDOT and PSS domains is reduced via surface tension, and the polymeric crystalline structures driven by π-π and lamella stacking (red parallel lines) are formed gradually but with random orientations (Figure 5a, ii). Similarly, the molecular scheme model for strain-engineered crystalline PEDOT:PSS microfibers which are prepared with the identical method except the drying process under the controlled stress (Figure 5b). Since the mechanical stress is applied to the as-spun *wet* microfiber during the drying process, the constituent polymeric chains could be gradually aligned along the fiber direction due to the existence of water molecules as lubricant and uniaxial stress via gravitational loads (Figure 5b, i). Subsequently, during water evaporation, the pre-aligned polymeric chains could be crystallized and the crystalline domains are aligned preferentially along the fiber direction (Figure 5b, ii). Note that since all fabrication procedures are identical except the introduction of mechanical stress before the complete drying, microfiber composition (*i.e.*, PEDOT/PSS ratio), thus, crystalline grain size, *d*-spacing (*i.e.*, x-ray peak positions), carrier density (*p*), volumetric capacitance

(C^*), and pinch-off voltage (V_p) should be the same for all PEDOT:PSS microfibers dried with/without mechanical stress, as shown in Figures 2c-e and 3e-g. Lastly, when two macroscopic schemes are compared with each other (Figure 5c-e), the applied voltage should produce an identical potential gradient between two ends of fibers. In the case of crystalline PEDOT:PSS microfibers prepared with the conventional method, randomly-oriented PEDOT grains generate the complicated tortuous pathway for charge transport with the lowest electrical resistance (Figure 5d). In contrast, when conjugated polymer chains were well aligned and crystallized preferentially along the fiber direction by strain-engineering, charge transport pathways are laid along the fiber direction which is the same as the direction of applied electric field due to the shortened pathway, so that the drift velocity of charged carriers could be enhanced at a given electric field, leading to the unprecedented increase (3 – 4 times) in hole mobility and μC^* product in comparison with randomly-oriented crystalline polymer fibers.

Conclusion

In summary, we successfully demonstrated high-performance microfiber-based OECTs with unprecedentedly large μ and μC^* by introducing strain-engineering into PEDOT:PSS microfibers in combination with solvent-mediated crystallization. The strain engineering via uniaxial tension was employed in the course of drying coagulated fibers after SA treatment, and the permanent preferential alignment of crystalline PEDOT:PSS domains along the fiber direction was verified by AFM and TR-WAXD. The resultant strain-engineered microfibers exhibited very high carrier mobility (12.9 $cm^2 V^{-1} s^{-1}$) without the trade-off in volumetric capacitance (122 F cm^{-3}) and hole density (5.8×10^{20} cm^{-3}). Such advantageous electrical and electrochemical characteristics enabled the bench-mark performance parameter of μC^* over ~1500 F $cm^{-1}V^{-1}s^{-1}$, which, to our knowledge, is the highest metric ever reported in the literature. We expect that the strain-engineering could be beneficial for realizing a new class of

323 substrate-free fibrillar and/or textile bioelectronics in the configuration of electrochemical transistors or

324 electrochemical ion pumps.

325

326

Acknowledgements

This work was supported by a National Research Foundation (NRF) grant funded by the Korean government (MSIT) (NRF-2017R1A2B4003873, NRF-2018M3A7B4070988, NRF-2020M3D1A1030660 and NRF-2020M1A2A2080748) and GIST Research Institute (GRI) in 2020. B.P. and J.R. gratefully acknowledge support from the National Science Foundation Grant No. NSF DMR-1751308.

Materials and Methods

Materials

Aqueous PEDOT:PSS solution (PH1000) and coagulation/crystallization chemicals (*i.e.*, acetone (EP grade) and sulfuric acid (EP grade)) were purchased from Heraeus and Duksan chemical, respectively. Au metal wires (>99.95%, 0.05, 0.1, and 0.5 mm diameter) for gravitational loads and silver wires (99.9%, 0.5 mm diameter) for gate electrode were purchased from Alfa Aesar.

Preparation of the strain-engineered PEDOT:PSS microfibers

Aqueous PEDOT:PSS solution was concentrated up to ~4 wt.% by using rotary evaporator (Hahnshin Scientific, HS-2005V-N), and filtered through a syringe filter (1.2 μm pore, Sartorius, 17593). The concentrated PEDOT:PSS solution was injected into the acetone-filled coagulation bath (500 mL) with a pumping rate of 2 mL/hr by using a syringe pump (New era pump systems, NE-300) and 30G stainless steel needles. The coagulated PEDOT:PSS microfibers were carefully rinsed with deionized water several times, and immersed into the concentrated sulfuric acid over 12 hrs. Subsequently, the SA-treated PEDOT:PSS microfibers were rinsed with deionized water by immersing microfibers into the 1-L water bath (10 min) and repeating this process five times, and the pre-weighed metal wire (Radwag, MYA 2.4Y, m= 0.082, 0.624, 1.17, 2.37, 4.99, 22.6, 53.5, 106, 206, 338 and 501 mg) was attached at the

350 end of the as-prepared microfiber segment (5 – 10 cm) by drying one very end of a microfiber in the air
351 and letting it adhered onto the load. Then, the whole microfiber segments tethered with metal wires were
352 dried for 1-2 min in the ambient condition (relative humidity <50%, temperature ~21°C). Note that the
353 501 and 206 mg loads which correspond to 61 and 14 MPa are the maximum load before the breakage
354 of SA- and ACE-treated microfibers during the drying process, respectively.

355 **Surface topography, microstructure, and composition analyses**

356 Strain-engineered microfibers were fixed on to a glass slide with Kapton tape and the
357 corresponding surface morphologies were examined using atomic force microscope (AFM; Park
358 systems, XE-Bio) and non-contact mode AFM cantilever (Budget Sensors, TAP300Al-G). All images
359 were aligned long the vertical direction, flattened for fiber curvature removal, and resized with 1.2 μm ×
360 1.2 μm using an image processing software (Gwyddion).

361 Transmission wide-angle x-ray diffraction (TR-WAXD) measurements were performed at the 9A
362 U-SAXS beamline of Pohang Light Source-II (PLS-II), Pohang, Republic of Korea. The incident x-ray
363 from the in-vacuum undulator (IVU) are monochromated using Si(111) double crystals and focused at
364 the detector position using K-B type mirror, and 2D diffraction patterns were recorded with a 2D CCD
365 (Rayonix Ltd., MX170-HS). The wavelength of x-ray, sample-to-detector distance, and exposure time
366 were set to be 1.12 Å, 215 mm, and 10 sec, respectively. Strain-engineered PEDOT:PSS microfibers
367 were loaded at the in-vacuum chamber to obtain a clear 2D diffraction pattern without background noises
368 from air and window scattering. The diffraction angle was calibrated using the pre-calibrated sucrose
369 sample.[40]

370 X-ray diffraction measurement was conducted with Empyrean from Panalytical with Cu-radiation
371 source. Wet as-prepared SA-treated PEDOT:PSS microfiber bundles were loaded on a silicon wafer, and
372 XRD spectra were acquired (i) before drying, (ii) after drying, and (iii) after immersing with deionized
373 water.

X-ray photoelectron spectroscopy (XPS) analysis was conducted with K-Alpha XPS instrument (Thermo Fisher Scientific). All samples were prepared by pulverizing microfibers (frozen with liquid nitrogen) using mortar and pestle. All spectra were normalized with S *2p* peak of thiophene in PEDOT, and fitted with asymmetric/symmetric models.

Characterization of swelling behavior of microfibers

The swelling measurement was conducted as described in the following. First, the fluidic channel (width = 1.6 mm, length = 25.4 mm) was defined on a glass slide using a dicing saw (Disco, DAD320) followed by cleaning with acetone, isopropanol and deionized water. Next, after one end of an as-prepared PEDOT:PSS microfiber (length: 2-3 mm) was attached onto the surface of fluid channel, the glass slide is covered with the cover slip glass (Paul Marienfeld) using Kapton tape (Figure S5a). Finally, the change in microfiber dimension was monitored with optical microscopy in the dry state (upper) and ~10 min after water injection into the channel (lower) using strain-engineered (i) ACE- and (ii) SA-treated microfibers. Then, the microscope images were taken and processed using ImageJ software to extract the length (L) and diameter (D) of a given fiber at each state and the radial, axial, and volume swelling ratios (*i.e.*, D_{wet}/D_{dry}, L_{wet}/L_{dry} and V_{wet}/V_{dry}, respectively) were calculated (Figure S5c-e).

Fiber dimension measurements and electrical characterizations

The lengths of PEDOT:PSS microfibers used for organic electrochemical transistor fabrication and electrochemical impedance spectroscopy were measured by optical microscopy (Sunny optical technology, SZMN). To measure the cross-sectional areas, PEDOT:PSS microfibers were fixed with cold-mount resin (R&B Inc., CM-ERH-Thin), and one end of a given microfiber was exposed by grinding/polishing (R&B Inc., RB 209 Minipol). The optical images of cross-sectional areas were acquired with bright-field optical microscopy (Olympus, BX51) and analyzed by an image processing program (ImageJ).

397 Four metal pad patterns with the separation of 200 μm were defined by photolithography and
398 thermal evaporation (Cr (5 nm)/Au (45nm)). Next, the PEDOT:PSS microfibers were carefully laid on
399 the four metal pad pattern, and the close physical contact was induced using a manipulator. Conductivity
400 was extracted/calculated from the 4-probe measurement with microfiber dimensions considered by
401 applying 100 μA current through two outer metal pads, and measuring voltage between two inner metal
402 pads with a source-measure unit (Keithley, 2400).

403 **Electrochemical impedance spectroscopy**

404 Electrochemical impedance spectroscopy was conducted with electrochemical workstation
405 (Metrohm-autolab, PGSTAT 302N), using aqueous NaCl solution (100 mM) with silver/silver chloride
406 reference electrode and platinum mesh counter electrode with single sinusoidal signal from 0.1 to 100
407 kHz with E_{ac} = 25 mV at E_{dc} = 0 V. The spectrum was analyzed by Nova software using the equivalent
408 circuit model consisting of one series resistor (R_s), one parallel resistor (R_p), and one capacitor (C_p). C^*
409 was calculated by normalizing the extracted C_p with the corresponding microfiber volume.

410 **OECT fabrication and characterization**

411 Two Cu tapes were adhered on the glass slide (Paul Marienfeld, Microscope slides) with the
412 separation of 10 mm, and each end of strain-engineered microfibers was electrically connected onto Cu
413 tapes using silver paste (CANS, Elcoat P-100). The exposed metallic parts except the PEDOT:PSS
414 microfiber channel area ($L \sim 0.3 – 0.4$ cm) was passivated with Kapton tape and dielectric epoxy (Alteco,
415 F-301). While the microfiber channel was in contact with aqueous NaCl solution (100 mM) where the
416 silver wire chlorinated with 4% sodium hypochlorite solution for 10 min is immersed for gate electrode,
417 the characterization of OECT devices was conducted with two source-measure units (Keithley, 2400)
418 using the custom MATLAB code. V_G was swept from -0.4 to 0.8 V with V_D fixed at -0.8V for transfer
419 curve measurement, and V_D was swept from 0 to -0.8 V with V_G stepped from -0.4 to 0.8V with an

interval of 0.2 V for output curve measurement. V_P was determined from the x-axis intercept of linearly fitted curve at the saturation regime of V_G vs. $I_D^{1/2}$ plot (*i.e.*, $I_D^{1/2} \propto (V_G - V_P)$), and p was calculated by using V_P and C^* (*i.e.*, $C^* = p/V_p$). μ_{OECT} was determined from the slope of the first differentiated transfer curve (*e.g.*, g_m) at the saturation regime (*i.e.* $dI_D/dV_G = g_m = \mu_{OECT} \cdot C^* \cdot A/L(V_G - V_P)$. Transconductance as a function of frequency was measured in ambient using a National Instruments PXIe-1082 system with two NI PXIe-4143 source-measure units, two NI PXIe-4081 digital multimeters, and a PIXe-6363 DAQ all controlled by custom LabView code, while V_D was fixed at -0.8 V and V_G was set with the DC offset of -0.2 V and the superimposed sine wave of 10 mV amplitude.

429 **References**

430 [1] S. Inal, G. G. Malliaras, J. Rivnay, *Nature Communications* **2017**, *8*, DOI 10.1038/s41467-017-
431 01812-w.

432 [2] S. Park, S. W. Heo, W. Lee, D. Inoue, Z. Jiang, K. Yu, H. Jinno, D. Hashizume, M. Sekino, T.
433 Yokota, K. Fukuda, K. Tajima, T. Someya, *Nature* **2018**, *561*, 516.

434 [3] G. D. Spyropoulos, J. N. Gelinas, D. Khodagholy, *Science Advances* **2019**, *5*, eaau7378.

435 [4] J. Rivnay, P. Leleux, M. Ferro, M. Sessolo, A. Williamson, D. A. Koutsouras, D. Khodagholy,
436 M. Ramuz, X. Strakosas, R. M. Owens, C. Benar, J.-M. Badier, C. Bernard, G. G. Malliaras,
437 *Science Advances* **2015**, *1*, e1400251.

438 [5] D. Khodagholy, T. Doublet, P. Quilichini, M. Gurfinkel, P. Leleux, A. Ghestem, E. Ismailova, T.
439 Hervé, S. Sanaur, C. Bernard, G. G. Malliaras, *Nature Communications* **2013**, *4*, 1575.

440 [6] C. Yao, Q. Li, J. Guo, F. Yan, I.-M. Hsing, *Advanced Healthcare Materials* **2015**, *4*, 528.

441 [7] Y. Liang, M. Ernst, F. Brings, D. Kireev, V. Maybeck, A. Offenhäusser, D. Mayer, *Advanced*
442 *Healthcare Materials* **2018**, *7*, 1800304.

443 [8] Y. Kim, T. Lim, C.-H. Kim, C. S. Yeo, K. Seo, S.-M. Kim, J. Kim, S. Y. Park, S. Ju, M.-H. Yoon,
444 *NPG Asia Materials* **2018**, *10*, 1086.

445 [9] G. Scheiblin, R. Coppard, R. M. Owens, P. Mailley, G. G. Malliaras, *Advanced Materials*
446 *Technologies* **2017**, *2*, 1600141.

447 [10] X. Ji, H. Y. Lau, X. Ren, B. Peng, P. Zhai, S.-P. Feng, P. K. L. Chan, *Advanced Materials*
448 *Technologies* **2016**, *1*, 1600042.

449 [11] P. Lin, X. Luo, I.-M. Hsing, F. Yan, *Advanced Materials* **2011**, *23*, 4035.

450 [12] M. P. Ferro, L. Leclerc, M. Sleiman, B. Marchiori, J. Pourchez, R. M. Owens, M. Ramuz,
451 *Advanced Biosystems* **2019**, *3*, 1800249.

[13] C. Pitsalidis, M. P. Ferro, D. Iandolo, L. Tzounis, S. Inal, R. M. Owens, *Science Advances* **2018**, *4*, eaat4253.

[14] M. Ramuz, A. Hama, J. Rivnay, P. Leleux, R. M. Owens, *Journal of Materials Chemistry B* **2015**, *3*, 5971.

[15] J. Rivnay, M. Ramuz, P. Leleux, A. Hama, M. Huerta, R. M. Owens, *Applied Physics Letters* **2015**, *106*, 043301.

[16] S. Zhang, Y. Li, G. Tomasello, M. Anthonisen, X. Li, M. Mazzeo, A. Genco, P. Grutter, F. Cicoira, *Adv. Electron. Mater.* **2019**, *5*, 1900191.

[17] S. Zhang, E. Hubis, G. Tomasello, G. Soliveri, P. Kumar, F. Cicoira, *Chemistry of Materials* **2017**, *29*, 3126.

[18] N. Matsuhisa, Y. Jiang, Z. Liu, G. Chen, C. Wan, Y. Kim, J. Kang, H. Tran, H. Wu, I. You, Z. Bao, X. Chen, *Adv. Electron. Mater.* **2019**, *5*, 1900347.

[19] B. D. Paulsen, K. Tybrandt, E. Stavrinidou, J. Rivnay, *Nature Materials* **2020**, *19*, 13.

[20] A. Giovannitti, C. B. Nielsen, D.-T. Sbircea, S. Inal, M. Donahue, M. R. Niazi, D. A. Hanifi, A. Amassian, G. G. Malliaras, J. Rivnay, I. McCulloch, *Nature Communications* **2016**, *7*, 1.

[21] H. Sun, J. Gerasimov, M. Berggren, S. Fabiano, *J. Mater. Chem. C* **2018**, *6*, 11778.

[22] A. Giovannitti, I. P. Maria, D. Hanifi, M. J. Donahue, D. Bryant, K. J. Barth, B. E. Makdah, A. Savva, D. Moia, M. Zetek, P. R. F. Barnes, O. G. Reid, S. Inal, G. Rumbles, G. G. Malliaras, J. Nelson, J. Rivnay, I. McCulloch, *Chemistry of Materials* **2018**, *30*, 2945.

[23] C. B. Nielsen, A. Giovannitti, D.-T. Sbircea, E. Bandiello, M. R. Niazi, D. A. Hanifi, M. Sessolo, A. Amassian, G. G. Malliaras, J. Rivnay, I. McCulloch, *Journal of the American Chemical Society* **2016**, *138*, 10252.

[24] S. Inal, J. Rivnay, P. Leleux, M. Ferro, M. Ramuz, J. C. Brendel, M. M. Schmidt, M. Thelakkat, G. G. Malliaras, *Advanced Materials* **2014**, *26*, 7450.

[25] A. M. Pappa, D. Ohayon, A. Giovannitti, I. P. Maria, A. Savva, I. Uguz, J. Rivnay, I. McCulloch, R. M. Owens, S. Inal, *Science Advances* **2018**, *4*, eaat0911.

[26] H. Sun, M. Vagin, S. Wang, X. Crispin, R. Forchheimer, M. Berggren, S. Fabiano, *Advanced Materials* **2018**, *30*, 1704916.

[27] A. Giovannitti, D.-T. Sbircea, S. Inal, C. B. Nielsen, E. Bandiello, D. A. Hanifi, M. Sessolo, G. G. Malliaras, I. McCulloch, J. Rivnay, *Proceedings of the National Academy of Sciences* **2016**, *113*, 12017.

[28] J. Rivnay, S. Inal, B. A. Collins, M. Sessolo, E. Stavrinidou, X. Strakosas, C. Tassone, D. M. Delongchamp, G. G. Malliaras, *Nature Communications* **2016**, *7*, 11287.

[29] S.-M. Kim, C.-H. Kim, Y. Kim, N. Kim, W.-J. Lee, E.-H. Lee, D. Kim, S. Park, K. Lee, J. Rivnay, M.-H. Yoon, *Nature Communications* **2018**, *9*, DOI 10.1038/s41467-018-06084-6.

[30] K. E. Aasmundtveit, E. J. Samuelsen, L. A. A. Pettersson, O. Inganäs, T. Johansson, R. Feidenhans'l, *Synthetic Metals* **1999**, *101*, 561.

[31] J. Zhou, E. Q. Li, R. Li, X. Xu, I. A. Ventura, A. Moussawi, D. H. Anjum, M. N. Hedhili, D.-M. Smilgies, G. Lubineau, S. T. Thoroddsen, *J. Mater. Chem. C* **2015**, *3*, 2528.

[32] Y. Kim, A. Lund, H. Noh, A. I. Hofmann, M. Craighero, S. Darabi, S. Zokaei, J. I. Park, M.-H. Yoon, C. Müller, *Macromolecular Materials and Engineering* **2020**, *305*, 1900749.

[33] D. A. Bernards, G. G. Malliaras, *Adv. Funct. Mater.* **2007**, *17*, 3538.

[34] D. Khodagholy, M. Gurfinkel, E. Stavrinidou, P. Leleux, T. Herve, S. Sanaur, G. G. Malliaras, *Applied Physics Letters* **2011**, *99*, 163304.

[35] D. Khodagholy, J. Rivnay, M. Sessolo, M. Gurfinkel, P. Leleux, L. H. Jimison, E. Stavrinidou, T. Herve, S. Sanaur, R. M. Owens, G. G. Malliaras, *Nature Communications* **2013**, *4*, 2133.

[36] J. Rivnay, P. Leleux, M. Sessolo, D. Khodagholy, T. Hervé, M. Fiocchi, G. G. Malliaras, *Advanced Materials* **2013**, *25*, 7010.

[37] F. Hempel, J. K.-Y. Law, T. C. Nguyen, W. Munief, X. Lu, V. Pachauri, A. Susloparova, X. T. Vu, S. Ingebrandt, *Biosensors and Bioelectronics* **2017**, *93*, 132.

[38] A. G. Polyravas, V. F. Curto, N. Schaefer, A. B. Calia, A. Guimera-Brunet, J. A. Garrido, G. G. Malliaras, *Flexible and Printed Electronics* **2019**, *4*, 044003.

[39] X. Wu, A. Surendran, M. Moser, S. Chen, B. T. Muhammad, I. P. Maria, I. McCulloch, W. L. Leong, *ACS Appl. Mater. Interfaces* **2020**, *12*, 20757.

[40] R. C. Hynes, Y. L. Page, *Journal of Applied Crystallography* **1991**, *24*, 352.

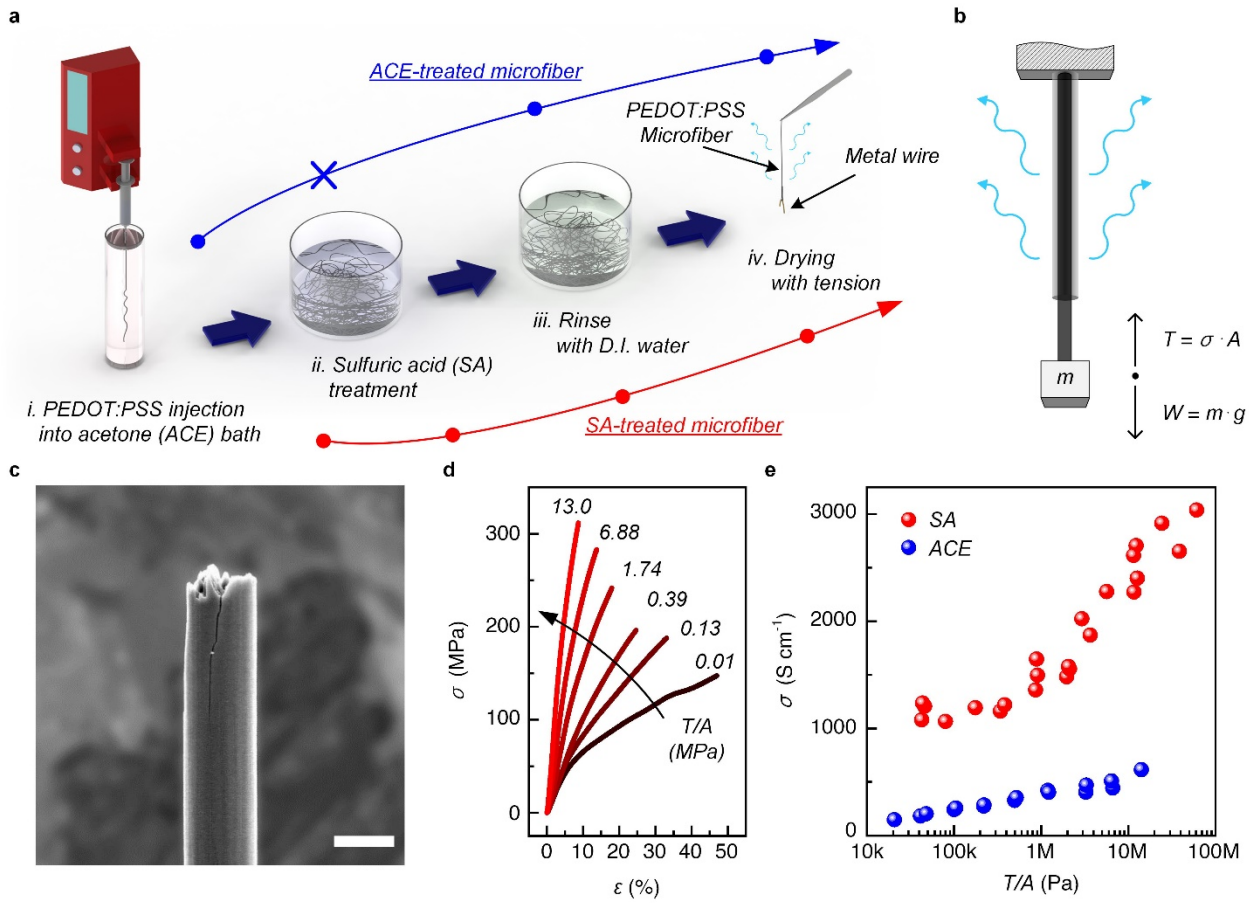

Figure 1. Preparation and basic characterizations of strain-engineered PEDOT:PSS microfibers. (a) Schematic illustration of wet-spinning, solvent-mediated crystallization (SA treatment), rinsing, and drying under tensile stress. Note that unlike the preparation of SA-treated microfibers (red arrow; lower row), that of ACE-treated microfibers (blue arrow; upper row) does not involve the SA treatment step. (b) A schematic of gravitational load-induced stress (*T*/*A*) during the drying process of an as-prepared fiber. (c) A representative SEM image of strain-engineered SA-treated PEDOT:PSS microfiber (the scale bar denotes 10 μm). (d) Stress-strain curves of SA-treated PEDOT:PSS microfibers. (e) Plots of conductivities of SA-treated (red) and ACE-treated (blue) microfibers as a function of the applied *T*/*A*.

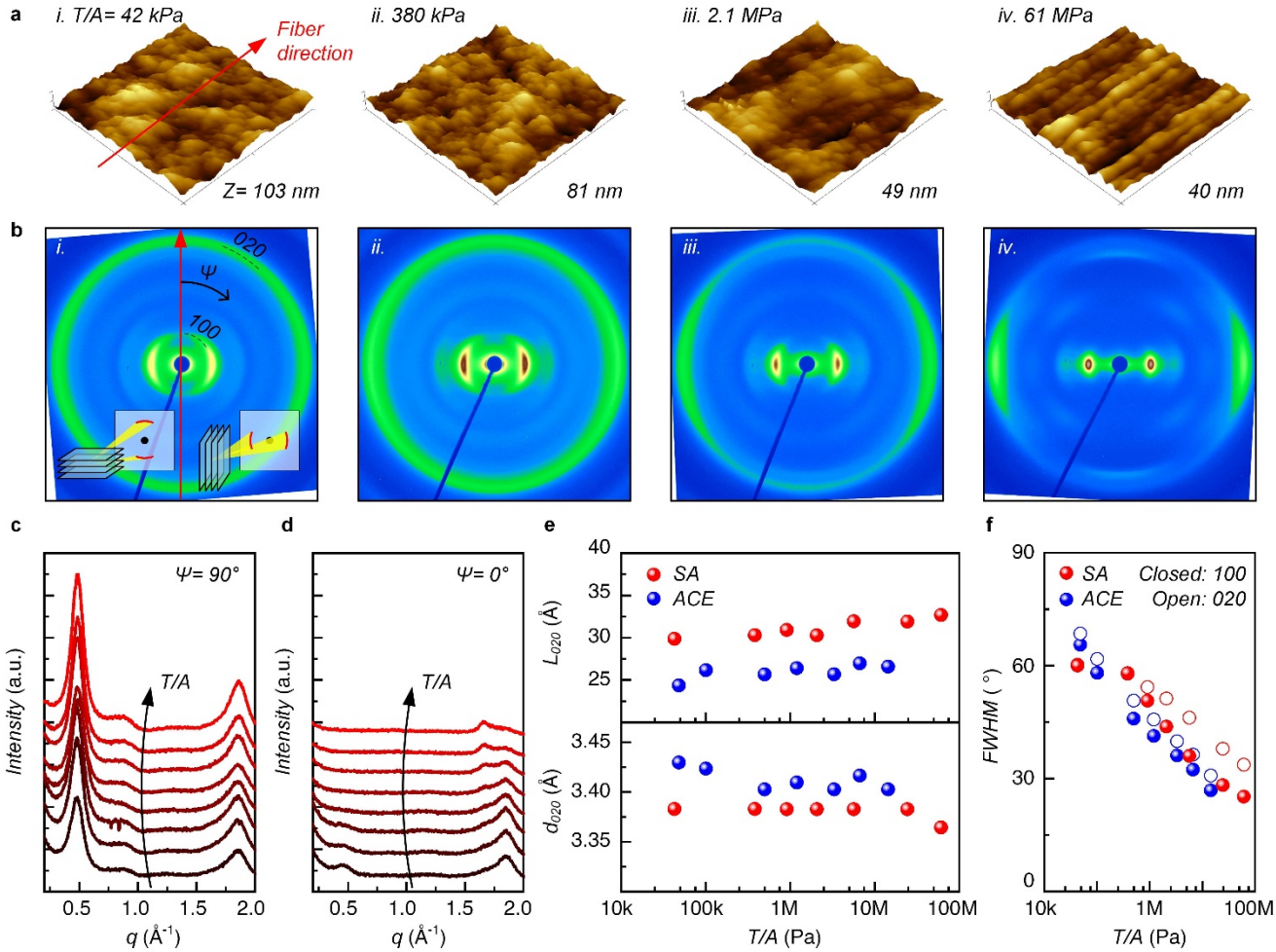

Figure 2. Anisotropically-ordered microstructures in strain-engineered PEDOT:PSS microfibers. (a) AFM surface topography images (1.2 μm × 1.2 μm) of and (b) TR-WAXD patterns of strain-engineered SA-treated microfibers (*T/A*: (i) 42 kPa, (ii) 380 kPa, (iii) 2.1 MPa, and (iv) 61 MPa). Red arrows indicate the fiber direction, and insets in (b) illustrate the peak orientations along the direction of crystallized stacks. Line profiles of TR-WAXD along (c) the vertical (ψ = 90°) and (d) parallel (ψ = 0°) axes of SA-treated microfiber. (e) Plots of grain size (L_{020}) and *d*-spacing (d_{020}) extracted from π-π stacking TR-WAXD peaks of SA-treated (red) and ACE-treated (blue) microfibers as a function of the applied *T/A*. (f) Plots of full width at half maximum (FWHM) values which were extracted from the azimuthal line cuts of TR-WAXD peaks (*i.e.*, (100; closed circles) and (020; open circles)) of SA-treated (red) and ACE-treated (blue) microfibers.

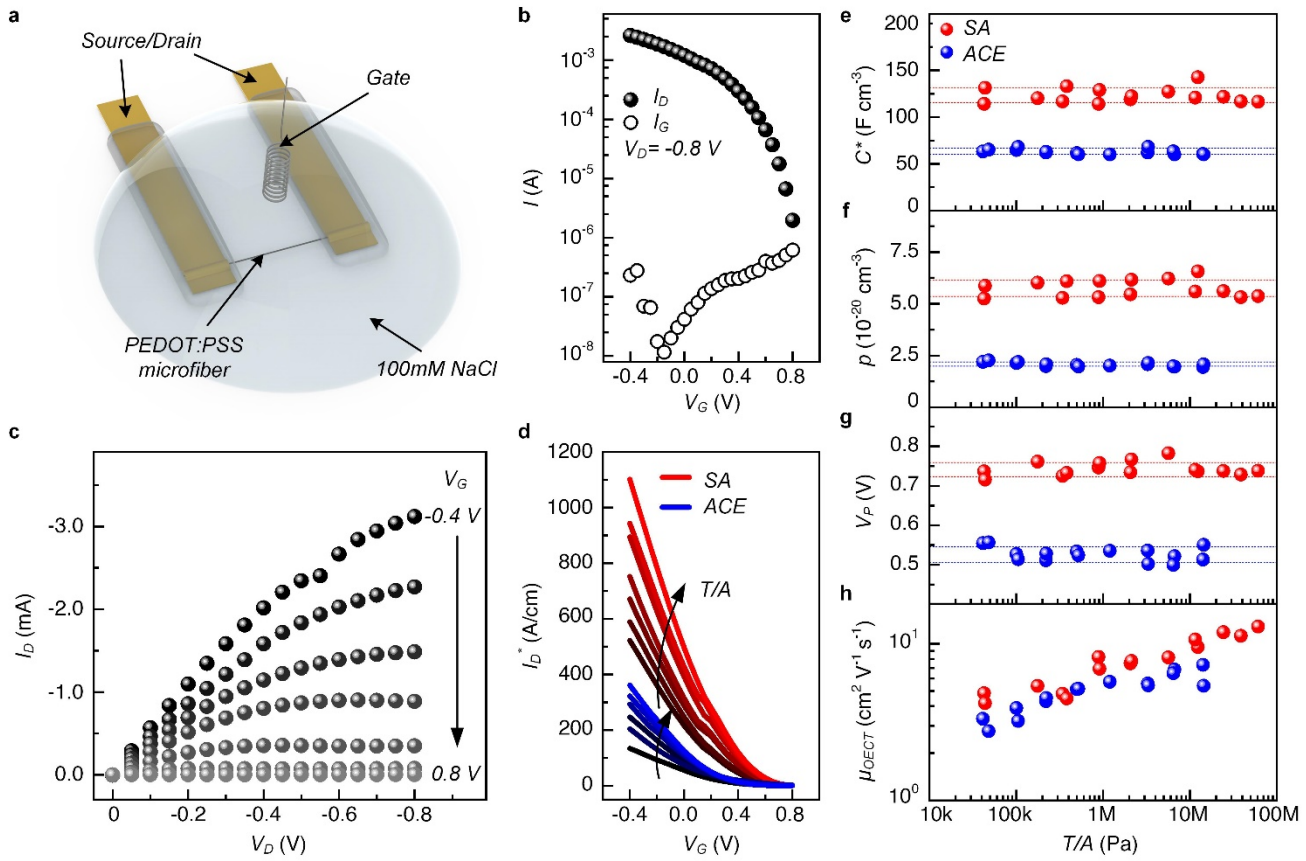

Figure 3. Strain-engineered PEDOT:PSS microfiber-based organic electrochemical transistors. (a) A schematic of microfiber organic electrochemical transistor. (b) Plots of representative transfer curves (V_G: -0.4 ~ 0.8, V_D: -0.8 V) and (c) output curves (V_D: 0 ~ -0.8V, V_G: -0.4 ~ 0.8V with 0.2 V step) from the strain-engineered microfiber OECT based on SA-treated PEDOT:PSS (T/A= 61 MPa, L/A= 0.33 cm/8.1 × 10^{-7} cm^2). (d) Plots of transfer curves using effective drain currents (I_D^*) which are normalized by microfiber dimensions for fair comparison ($I_D^* = I_D \cdot L/A$). Red and blue curves denote OECT transfer characteristics from strain-engineered SA-treated and ACE-treated microfibers, respectively, at various applied T/A coded with color gradient. Plots of representative electrical/electrochemical characteristics as a function of the applied T/A: (e) volumetric capacitance (C^*), (f) hole density (p), (g) pinch-off voltage (V_P), and (h) carrier mobility (μ_{OECT}) extracted from strain-engineered SA-treated (red) and ACE-treated (blue) PEDOT:PSS microfiber OECTs. Dotted lines indicate upper and lower standard deviation limits.

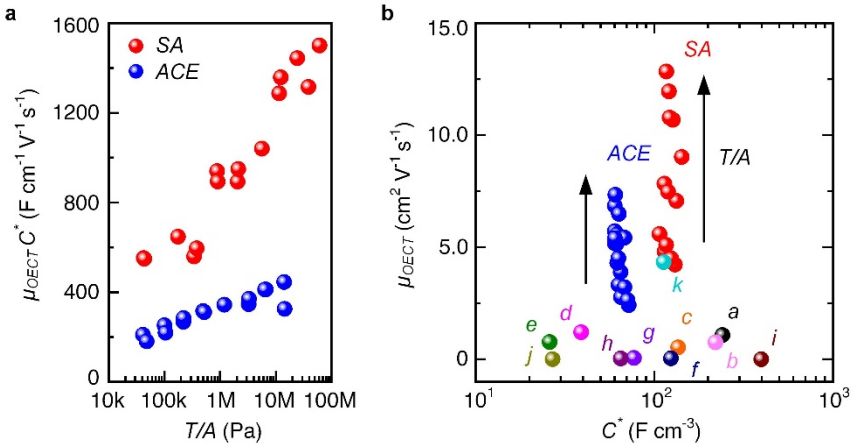

Figure 4. Benchmarking mixed conductor figure-of-merit (μC^*) and carrier mobility. (a) Plots of μC^* product of strain-engineered SA-treated (red) and ACE-treated (blue) PEDOT:PSS microfibers as a function of applied *T/A*. and (b) μ-C^* map for benchmarking organic mixed conductors including strain-engineered SA-treated (red) and ACE-treated (blue) PEDOT:PSS microfibers. Note that the $\mu(\mu_{OECT})$ and C^* values of previously-reported organic mixed conductors are referenced from the previous literature[1] . The detailed information is described in Table S1.

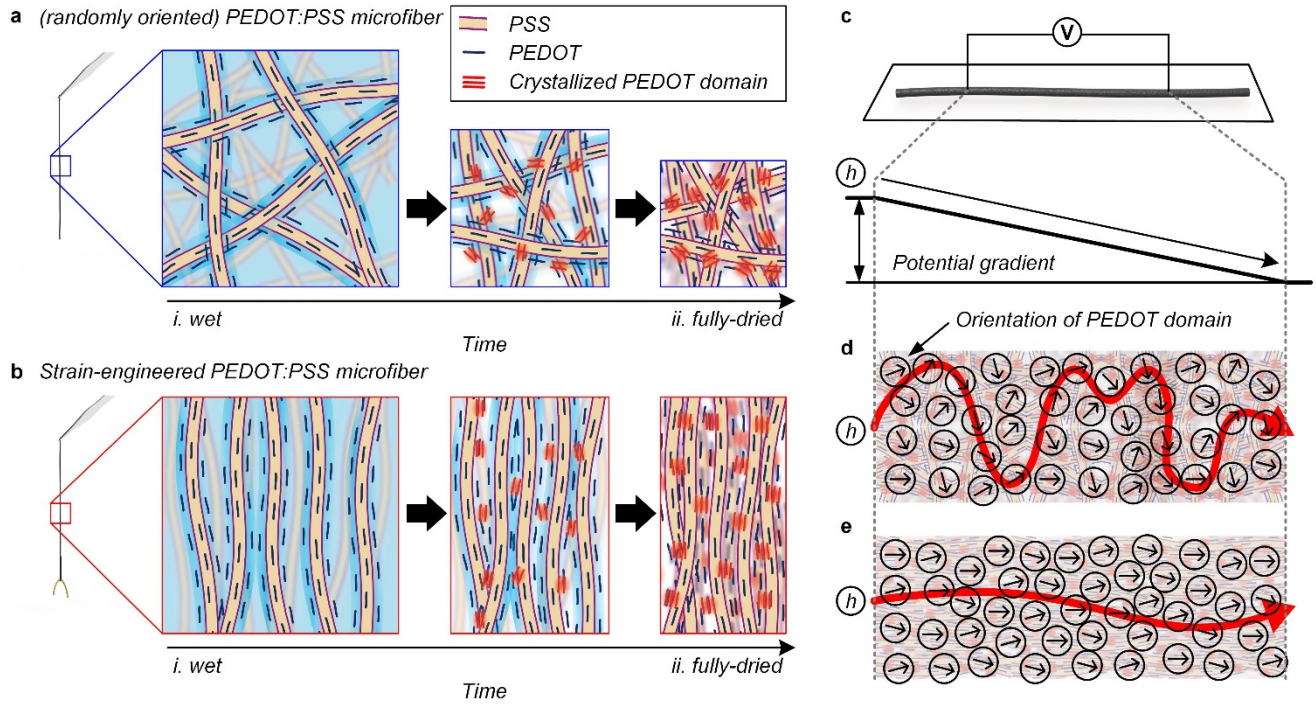

Figure 5. Proposed comparative mechanisms of anisotropic polymeric crystallite ordering and carrier mobility enhancement in strain-engineered crystalline PEDOT:PSS microfibers. Schematic illustration of structural evolution of *wet* PEDOT/PSS chains during the drying process (a) without and (b) with applied stress (*T/A*). Note that in the presence of uniaxial tension during the drying process, the constituent polymeric chains are gradually crystallized, and the resultant crystalline domains are aligned along the fiber direction. (c) A schematic of potential gradient applied between two ends of PEDOT:PSS microfiber. Proposed microstructures of (d) randomly-oriented polymeric crystallites in PEDOT:PSS microfiber prepared without applied *T/A*, and (e) preferentially-oriented polymeric crystallites along the fiber direction in strain-engineered PEDOT:PSS microfiber.